
S2MDF: A Plug-And-Play Layer for Intersection-Free Multi-Object Signed Distance Fields

Deniz Sayin Mercadier* Federico Stella* Aurel Bizeau Nicolas Talabot Pascal Fua
CVLab, Ecole Polytechnique Fédérale de Lausanne (EPFL)
Lausanne, Switzerland
{firstname.lastname}@epfl.ch

Abstract

Compositional implicit surface representations model scenes as collections of objects, each encoded by a Signed Distance Field (SDF). A fundamental limitation of this approach is that multiple SDFs can produce geometries that interpenetrate, violating physical plausibility. Existing mitigation strategies rely on soft penalty terms that reduce but do not eliminate intersections, and require careful loss weighting. To truly prevent interpenetration, we propose a hard constraint on vector-valued SDFs and introduce S2MDF, a lightweight plug-and-play module that enforces the constraint on any object-compositional SDF representation without architectural modifications. It introduces negligible computational overhead and is compatible with linearly-interpolated standard meshing algorithms such as Marching Cubes. It can be applied during training or as a post-processing step. Experiments on multiple state-of-the-art compositional methods show that S2MDF reduces intersections to numerical precision while preserving reconstruction quality, outperforming existing mitigation strategies.

1 Introduction

Over the past few years, implicit neural representations (INRs) have reshaped the landscape of 3D vision and graphics. By encoding geometry or appearance as continuous functions parameterized by neural networks, methods such as DeepSDF [39], 3DShape2VecSet [69], NeRF [34], NeuS [57] and their many extensions have demonstrated remarkable performance in tasks such as novel view synthesis [50], high-fidelity surface reconstruction [16], shape generation [26], manipulation [20] and optimization [21]. Unlike older discrete representations such as meshes and voxels, INRs provide resolution-independent modeling, differentiability, and a natural framework for learning complex geometric priors. This paradigm shift has fostered significant progress in fields as diverse as robotics, medical imaging, and digital content creation, where accurate and flexible 3D representations are paramount.

As these methods mature, a growing body of work has focused on extending INRs beyond single-object descriptions towards more realistic multi-object representations of scenes [60, 51, 61] and multi-part models of composite objects [12, 41, 49]. These are particularly valuable for downstream tasks such as manipulation, simulation, and design, where reasoning about individual entities or parts is key. For example, when designing the 3D shape of a car to improve its aerodynamics, one has to consider its body, its wheels, and all the accessories that are usually attached to it. Similarly, when modeling a heart from medical imagery, one should consider its four chambers and the blood vessels attached to them. Numerous object-compositional implicit representations [73, 71, 30, 61, 49, 27] have been introduced to this end. A common approach is to rely on a set of Signed Distance Fields (SDF) [57], one per object [60, 61, 49], and to combine them appropriately.

*Equal contribution.

While effective and popular, this approach faces a fundamental challenge: Even though physical objects cannot share the same volume in space, multiple SDFs can easily produce configurations that violate this. A number of strategies have been proposed to mitigate this problem. They include minimizing loss terms that penalize overlap [49], visibility-based constraints to handle occlusions [61], and regularization techniques inspired by physical reasoning [27]. While these approaches reduce the frequency and severity of intersections, they do not guarantee their complete removal. Furthermore, because the intersection loss terms are usually minimized as part of a weighted sum of several other loss terms, careful tuning of their respective weights is often required.

In this work, we propose an approach that strictly prevents intersections without needing a weighting scheme. To this end, we define a hard-constraint on vector-valued SDFs that produces an intersection-free geometry. We will refer to such a constrained field as a *Multi-object Distance Field (MDF)*. Given this formalism, we implement *S2MDF*, a simple yet effective module that enforces the constraint and can be seamlessly integrated into existing pipelines with a negligible computational overhead. It can be applied either during training or as a post-processing step to enforce the intersection-free constraint on virtually any object-compositional SDF-based representation, without requiring any architectural change. Furthermore, it remains compatible with standard linearly-interpolated meshing techniques such as Marching Cubes [32] and Marching Tetrahedra [5].

To summarize our contributions:

- We formalize the problem of generating intersection-free multi-object implicit surface representations by constraining vector-valued SDFs to encode intersection-free geometry as a Multi-object Distance Field (MDF);
- We propose S2MDF, a fast, plug-and-play module that projects object-compositional SDF-based representations into an MDF, ensuring intersection-free geometry with negligible computational overhead.

We validate our approach on several state-of-the-art SDF-based object-compositional methods, demonstrating that S2MDF, paired with existing linearly-interpolated meshing techniques, reduces intersections to numerical precision while preserving reconstruction quality. Through both qualitative and quantitative evaluations, we show that our method outperforms existing mitigation strategies and provides a robust, generic solution to a longstanding limitation of compositional neural surface representations.

2 Related work

We first put Implicit Neural Representations in the more general context of representing the 3D shape of single objects and then briefly review existing approaches to jointly model several objects.

Representing the Shape of 3D Objects. Many different representations have been proposed over the years. Voxel-based methods represent the space as a grid [63, 59, 10, 11], but suffer from high memory requirements and limited resolution. Point-cloud-based methods represent surfaces as sets of points [15, 65, 1, 40, 67], which improves the memory footprint but ignores connectivity, as they do not explicitly model the surface as a continuous entity. Mesh-based methods represent surfaces as collections of vertices, edges and faces [17, 56, 23, 38], which allows for efficient rendering and manipulation, but generally require a fixed topology that is difficult to modify. Implicit Neural Representations represent a powerful alternative, encoding geometry as continuous functions parameterized by neural networks [39, 33, 8]. Among these, Signed Distance Fields (SDFs) and occupancy fields are particularly popular for representing watertight surfaces, which can then be extracted from the field using standard meshing techniques [32, 13, 28, 22]. When the surface is not watertight, Unsigned Distance Fields (UDFs) can be used instead [9, 31, 29], with specially designed meshing techniques [19, 70, 46]. Differentiability between the explicit surface and the field can be achieved thanks to the implicit function theorem, whose practical viability has been shown for both SDFs [43, 18] and UDFs [19], allowing shape optimization tasks such as drag reduction. Recent works extend these approaches using new latent spaces [48, 35, 68, 69] and more complex network architectures [72, 6], allowing for highly detailed generative modeling and shape manipulation.

Handling Multiple Objects Jointly. Object-aware implicit representations have been proposed in the context of NeRFs [37, 51], often involving a separate semantic branch to predict object labels [55, 14], and in some cases two separate radiance fields, one for the scene and for the objects [64]. However these approaches do not directly model geometry. ObjectSDF [60] and

ObjectSDF++ [61] are among the first works to propose object-compositional implicit surface representations, where multiple SDFs are used to represent different objects. ObjectSDF [60] defines an approach to directly render the semantic field, coupling semantics and geometry, while ObjectSDF++ [61] supervises the geometry with semantic information and adds a loss term to penalize object collisions. However, neither approach prevents interpenetrations between objects. Part-based generative models [62, 12, 41] represent individual parts of objects but typically output independent, potentially non-physical, SDFs. The more recent PartSDF [49] proposes a single decoder to produce all fields jointly, with a loss term to penalize intersections, but again without guarantees. Other works in the medical and robotics domains, where physical plausibility is key, also use special losses to reduce penetration between parts [24, 71, 27], while sometimes enforcing contact [27], but they either do not guarantee the absence of intersections or they are not based on INRs. Instead, we propose a simple module that can be applied to any object-compositional SDF-based representation, either during training or as a post-processing step, to prevent interpenetration while preserving the quality of the reconstructions.

3 Method

Signed Distance Fields (SDFs) naturally represent single, watertight, objects by encoding the positive or negative distance to the closest surface for each point in space, the typical convention being that negative values are inside the object and positive ones outside. For a watertight object O and its boundary ∂O , this can be written as

$$SDF_O : \mathbb{R}^3 \rightarrow \mathbb{R}, \quad SDF_O(\mathbf{p}) = \begin{cases} -\min_{\mathbf{q} \in \partial O} \|\mathbf{p} - \mathbf{q}\|, & \text{if } \mathbf{p} \in O \\ \min_{\mathbf{q} \in \partial O} \|\mathbf{p} - \mathbf{q}\|, & \text{if } \mathbf{p} \notin O \end{cases} \quad (1)$$

In an object-compositional setting, each one of K object is typically assigned its own SDF_k for $1 \leq k \leq K$ and we can define the composite $SDF = [SDF_1, \dots, SDF_K] : \mathbb{R}^3 \rightarrow \mathbb{R}^K$. The problem with this is that each SDF is independent from the others: Nothing stops two of the SDF_k from returning negative values at the same spatial location, which would mean that this location is inside two different objects, a configuration that should not be allowed. This is what we want to achieve by appropriately constraining SDF . We first formalize this constraint and then discuss various approaches to enforcing it.

3.1 Multi-Object Signed Distance Fields

Let $\min^{(n)}(\cdot)$ be the operator that returns the n -th smallest element of its input vector. Given a spatial location \mathbf{p} , let $\mathbf{u} = SDF(\mathbf{p})$ be its vector-valued composite SDF. To ensure that \mathbf{p} is not inside more than one object it should satisfy

$$\min^{(2)}(\mathbf{u}) \geq 0. \quad (2)$$

This constraint ensures that the second smallest signed distance value at any point is non-negative, which means that at most one of the SDF_k can be negative at any location. If we could truly enforce it everywhere, this would be enough. But, in practice, we have to sample the space more or less densely and we can only enforce the constraint at those sample points. Furthermore, the deep networks used to implement the SDF_k functions do not guarantee that they satisfy the eikonal property $\|\nabla SDF_k\| = 1$. Taken together, these two limitations mean that SDF approximations can satisfy the constraint of Eq. (2) on sample points and yet produce interpenetrations, as shown in Fig. 1a. To remedy this, we propose to use an equivalent constraint based on the following theorem

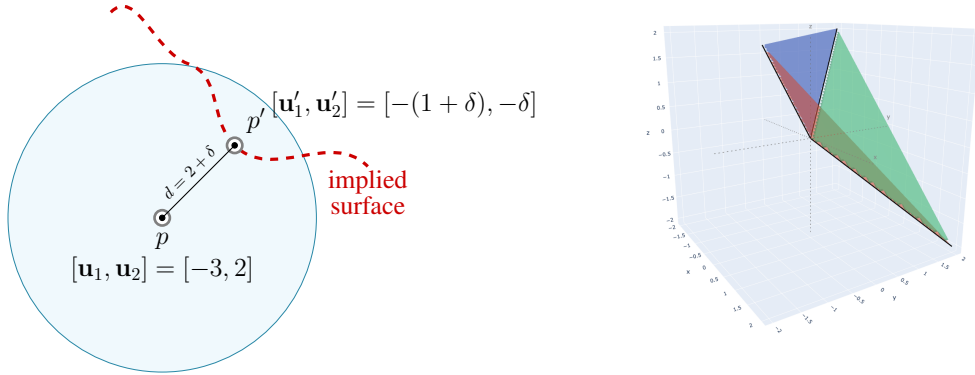
Theorem 1. *A vector-valued $SDF = [SDF_1, \dots, SDF_K] : \mathbb{R}^3 \rightarrow \mathbb{R}^K$ satisfies constraint 2 at every point $\mathbf{p} \in \mathbb{R}^3$, with $\mathbf{u} = SDF(\mathbf{p})$, if and only if it satisfies the following constraint at every point $\mathbf{p} \in \mathbb{R}^3$:*

$$\min^{(1)}(\mathbf{u}) + \min^{(2)}(\mathbf{u}) \geq 0. \quad (3)$$

Proof: Appendix A.2.1, using Lipschitz continuity of true SDFs.

This constraint is visualized in Fig. 1b. Even though Eq. (2) and Eq. (3) are equivalent for true SDFs, the second constraint is *stronger* for neural, imperfect SDFs. In fact, the following holds:

Theorem 2. *Given two points $\mathbf{p}_1, \mathbf{p}_2 \in \mathbb{R}^3$ and an arbitrary vector-valued function $f : \mathbb{R}^3 \rightarrow \mathbb{R}^K$ evaluated at those points, $\mathbf{u}_1 = f(\mathbf{p}_1)$ and $\mathbf{u}_2 = f(\mathbf{p}_2)$ that satisfy constraint 3, then the constraint*



(a) Given a point \mathbf{p} inside the circle and its SDF \mathbf{u} satisfying $\min^{(2)}(\mathbf{u}) \geq 0$, there is an implication of a nearby point \mathbf{p}' with SDF \mathbf{u}' having both entries negative, thus $\min^{(2)}(\mathbf{u}') \not\geq 0$. This value of \mathbf{u} would not be allowed if Eq. Eq. (2) was satisfied everywhere.

(b) Illustration of the feasible space for the MDF constraint in Eq. Eq. (3) for $K = 3$ objects: an intersection of $C(K, 2)$ hyperplanes in \mathbb{R}^K delimits the feasible region on the right. Each plane corresponds to the constraint imposed by the sum of one pair of SDFs.

Figure 1: Illustrations of properties related to the constraints in Eqs. Eq. (2) and Eq. (3).

is also satisfied for every point along the line segment connecting \mathbf{p}_1 and \mathbf{p}_2 , where intermediate vectors are obtained via linear interpolation as $\mathbf{u}_\alpha = \alpha\mathbf{u}_1 + (1 - \alpha)\mathbf{u}_2$ for $\alpha \in [0, 1]$. *Proof: Appendix A.2.3.*

In other words, a linear interpolation of an imperfect SDF that satisfies constraint 3 on a finite set of points, also satisfies the constraint everywhere. The same is not true for constraint 2. This is important because, as mentioned above, SDF parametrizations are not perfect, and are often evaluated at a finite number of points and interpolated in between, for example by iso-surface extraction algorithms. Thus the formulation of Theorem 1 is the one we use in practice and we define our Multi-object Distance Fields as follows:

Definition 1. A Multi-object Distance Field (MDF) is a vector-valued SDF $\mathbb{R}^3 \rightarrow \mathbb{R}^K$ that maps each point in space to a vector of K signed distance values, one for each of K objects, and satisfies the constraint of Eq. (3).

3.2 Enforcing the MDF Constraint

Given a vector-valued SDF, independently from its parametrization, we want to ensure that the K -dimensional vector $\mathbf{u} = SDF(\mathbf{p})$ meets the constraint of Eq. (3) for all \mathbf{p} it is evaluated at. The natural way to do this is to perform a projection, that is, replace \mathbf{u} by the vector \mathbf{d} that is closest to \mathbf{u} and meets the constraints. We write this as

$$\text{minimize} \|\mathbf{d} - \mathbf{u}\|^2 \quad \text{subject to} \quad \min^{(1)}(\mathbf{d}) + \min^{(2)}(\mathbf{d}) \geq 0. \quad (4)$$

Theorem 2 ensures that the linear interpolation of those samples satisfies the MDF constraint. Thus Eq. (4) gives us a separate problem to solve for each sample point. As we normally perform computations on batches of points, the solution must be regular enough to be easy to parallelize for a fast computation. When $K = 2$, Eq. (4) has a simple analytical solution and this is no issue. However, for $K > 2$, the non-linearity of $\min^{(1)}$ and $\min^{(2)}$ becomes one and there are no standard solvers that can be used for our purposes. We implemented two distinct solutions to this problem.

3.2.1 Quadratic Programming

The minimization of Eq. (4) is subject to a non-linear constraint but we can rewrite it as

$$\text{minimize} \|\mathbf{d} - \mathbf{u}\|^2 \quad \text{subject to} \quad d_i + d_j \geq 0, \quad 1 \leq i < j \leq K. \quad (5)$$

We prove in Appendix A.2.2 that the constraints of Eqs. (4) and (5) are *strictly* the same, meaning the problem and by extension its solutions are the same. While the formulation of Eq. (5) may

seem more complex, it has the advantage to be a standard Quadratic Program (QP) for which there are mature solvers [2, 3] whose solution can be readily differentiated. Thus, they can be directly integrated inside neural networks for an acceptably small runtime cost as long as K is not too large. In our implementation, we embed one in the final layer of the neural network parameterizing all the signed-distance values, effectively projecting SDF values onto the manifold of intersection-free MDFs.

3.2.2 Analytical Solution

The drawback of our QP formulation is that the number of constraints, and by extension the runtime cost of solving the problems, scales quadratically with the number of objects K , which can become prohibitive, especially during training when they are invoked at every iteration. This can be addressed using the following heuristic. When $K = 2$, the analytical solution to Eq. (4) is to add $-(\min^{(1)}(\mathbf{u}) + \min^{(2)}(\mathbf{u}))/2$ to each \mathbf{u} , see Appendix A.2.5 for the proof. When $K > 2$, we can still replace each \mathbf{u} by

$$\text{Shift-All}(\mathbf{u}) = \begin{cases} \mathbf{u} & \text{if } \min^{(1)}(\mathbf{u}) + \min^{(2)}(\mathbf{u}) \geq 0, \\ \mathbf{u} - \frac{\min^{(1)}(\mathbf{u}) + \min^{(2)}(\mathbf{u})}{2} & \text{otherwise.} \end{cases} \quad (6)$$

This is no longer the optimal solution to the problem of Eq. (4), but it is a feasible one, and we show in Appendix A.2.6 that it is the solution to the problem of Eq. (4) under the additional constraint that the pairwise differences between the different SDF values be preserved, a reasonable constraint to avoid disrupting the ordering of the original fields during the projection. It has the added benefit to be much simpler and faster to compute than solving the QP problem.

This mapping is continuous, differentiable almost everywhere, and the non-differentiable points are typically not on the object surfaces. In other words, it does not create issues either for meshing or training, unlike the non-differentiability of Unsigned Distance Fields on the surface that is well known to create problems [19, 70, 46]. Moreover, being an optimal solution to problem 4 does not necessarily mean that the QP solution is better in practice, as optimality is defined in terms of the L_2 distance to the original vector \mathbf{u} , which is an arbitrary metric. In practice, we show in the results section that this heuristic performs equally well as the QP solution, and even better in some cases, at a much lower computational cost.

3.3 Meshing

If explicit representations are required by downstream applications, our MDF needs to be turned into multi-object 3D meshes that preserve their non-intersecting nature. Doing this for standard SDFs usually relies on isosurface extraction algorithms such as Marching Cubes [32, 28], Marching Tetrahedra [5, 52], or Dual Contouring [22]. When dealing with multiple SDFs, these algorithms are often applied independently to each SDF, and the resulting meshes are interpreted as lying in the same physical space, with potential intersections. A partial exception to this is Dual Contouring, for which a multi-object-aware version exists [42], but we do not know of any readily accessible implementation of this algorithm.

Fortunately, this is not an issue thanks to Appendix 2 that states that the linear interpolation of an MDF is still an MDF. This guarantees that, when the MDF constraint is satisfied at the grid points, it is possible to extract intersection-free meshes using linearly interpolated meshing algorithms, including their adaptive variations [44], on each SDF independently, as we prove in Sec. A.2.4. In other words, we can use some of the existing meshing methods as they are, on each MDF component independently.

4 Experiments

Our approach is designed to be generic and usable in conjunction with any signed distance function. To demonstrate this, we use it to impose non-intersection constraints on three modern multi-object modeling techniques [61, 27, 49], some of which come with their own approaches to addressing the problem. This allows for comparisons between the different variants of our intersection prevention method and theirs, and shows the effectiveness of our method across different architectures, tasks and domains. We present the methods below.

Data	Model	MCD ($\times 10^{-4}$) ↓	MNC ↑	F1 (0.01) ↑	IoU ↑	IV ↓
TS-Lung (Both)	Vanilla MedTet	5.462 ± 0.118	96.729 ± 0.059	99.601 ± 0.008	93.737 ± 0.038	2.755 ± 0.767 ($\times 10^{-4}$)
	S2MDF (QP) - PP	5.800 ± 0.314	96.766 ± 0.004	99.575 ± 0.035	94.011 ± 0.850	1.190 ± 0.407 ($\times 10^{-6}$)
	S2MDF (QP) - Train	5.357 ± 0.309	96.791 ± 0.019	99.594 ± 0.007	94.255 ± 0.033	1.907 ± 0.444 ($\times 10^{-7}$)
	S2MDF (Shift-All) - PP	5.600 ± 0.289	96.708 ± 0.023	99.579 ± 0.036	94.000 ± 0.207	1.132 ± 0.245 ($\times 10^{-6}$)
	S2MDF (Shift-All) - Train	5.394 ± 0.056	96.788 ± 0.055	99.620 ± 0.010	93.863 ± 0.397	1.391 ± 0.934 ($\times 10^{-7}$)
MMWHS (Heart)	Vanilla MedTet	23.863 ± 1.330	94.333 ± 0.157	97.470 ± 0.142	83.580 ± 0.473	3.445 ± 1.390 ($\times 10^{-4}$)
	S2MDF (QP) - PP	29.420 ± 4.430	94.293 ± 0.062	97.367 ± 0.073	83.591 ± 0.081	8.446 ± 3.149 ($\times 10^{-11}$)
	S2MDF (QP) - Train	24.796 ± 0.670	94.386 ± 0.106	97.465 ± 0.308	83.544 ± 0.481	2.674 ± 3.486 ($\times 10^{-9}$)
	S2MDF (Shift-All) - PP	31.099 ± 7.072	94.316 ± 0.151	97.297 ± 0.229	83.694 ± 0.375	9.888 ± 1.793 ($\times 10^{-12}$)
	S2MDF (Shift-All) - Train	23.094 ± 0.331	94.407 ± 0.089	97.556 ± 0.173	83.901 ± 0.039	4.635 ± 5.606 ($\times 10^{-11}$)

Table 1: Experimental results on MedTet. Means are across all organ components and samples, averaged over runs with 3 different random seeds.

	MCD ($\times 10^{-2}$) ↓	NC ↑	F1 (0.01) ↑	IV ↓
Vanilla ObjectSDF++ (MC)	5.115 ± 15.586	0.781 ± 0.102	0.858 ± 0.143	1.496 ± 3.821 ($\times 10^{-3}$)
QP (MC)	2.620 ± 10.407	0.781 ± 0.102	0.871 ± 0.138	1.088 ± 5.380 ($\times 10^{-4}$)
Shift (MC)	2.711 ± 10.825	0.781 ± 0.102	0.870 ± 0.138	1.169 ± 4.505 ($\times 10^{-7}$)
S2MDF (Shift-All) - Train	4.795 ± 26.764	0.768 ± 0.110	0.860 ± 0.153	2.436 ± 10.266 ($\times 10^{-7}$)
S2MDF (Shift-All Skip-Conn.) - Train	1.847 ± 24.549	0.768 ± 0.102	0.829 ± 0.171	2.877 ± 25.094 ($\times 10^{-7}$)

Table 2: ObjectSDF++ [61] trained for object-compositional 3D scene reconstruction on 8 Replica [47] scenes. Mean and standard deviation across scenes and objects, weighted by the number of objects per scene. Background mesh has been excluded from the evaluation due to the presence of large flat surfaces outside of the scenes across all methods, which would skew the metrics and make them less informative.

4.1 Target Methods

MedTet [7] is a medical imaging model designed to perform 3D organ reconstruction from CT/MRI scans using the Deep Marching Tetrahedra [45] algorithm. The model learns to deform and predict SDF values per-vertex on a tetrahedral grid, and then extracts surfaces using Marching Tetrahedra. Losses can be applied both on SDF predictions and the extracted mesh thanks to the surface extraction being differentiable. It does not include any intersection-mitigating mechanisms. We evaluate MedTet in Tab. 1 and 4 on two datasets:

MM-WHS [74]: a dataset for whole heart segmentation, containing 20 annotated CT samples with 7 heart components – left ventricle, right ventricle, left atrium, right atrium blood cavities, left ventricle myocardium, aorta and pulmonary artery.

TS-Lung [58]: the lung component of the TotalSegmentator dataset, containing 318 lung CT scans with 5 parts: 2 lobes of the left lung and 3 lobes of the right lung. While lung segmentation is considered a simple task with many approaches being able to achieve very high Dice scores [53], we find this dataset useful due to the large number of samples present and the possibility of multi-way intersections.

ObjectSDF++ [61] is a neural implicit framework designed for high-fidelity, object-compositional 3D scene reconstruction. It utilises an occlusion-aware opacity rendering to reconstruct a scene as a collection of distinct, individual objects alongside a separate background. It includes an intersection-mitigating loss which substantially degrades the method if not used [61], so we do not ablate it. We evaluate the model for scene reconstruction using the Replica [47] dataset, adapted from MonoSDF [66]. Our evaluation covers 8 distinct scenes and is carried out as in the original paper, with each scene comprising dozens of individual objects, including the background. The ground-truth meshes used to compute our evaluation metrics are extracted with the vMAP framework [25]. We extract the meshes with Marching Cubes at resolution 256. The results are presented in Tab. 2 and Fig. 2, excluding the IoU metric which cannot be computed in this setting due to non-watertight ground-truth meshes.

PartSDF [49] is an SDF-based method for part-aware shape representation, with applications in shape reconstruction, generation and optimization. It represents shapes as a collection of parts, each represented by a separate SDF, and includes a loss term to mitigate intersections between parts akin to [61, 27]. We follow the experimental setup of the original paper for shape reconstruction and train

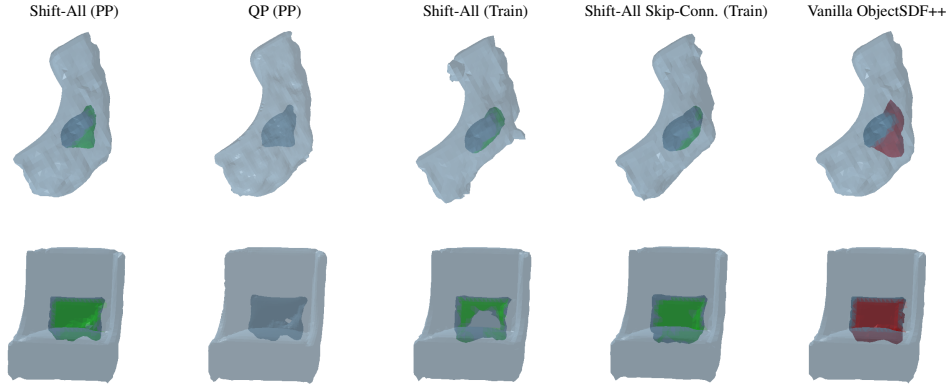


Figure 2: Transversal (top) and frontal (bottom) views of a chair (light grey) and a pillow (dark grey) from Room 0 of the Replica dataset, reconstructed under five scenarios for ObjectSDF++ [61], illustrating inter-object intersections in red and contacts in green. The vanilla version has significant intersections, while the constrained versions do not.

Data	Model	MCD ($\times 10^{-4}$) \downarrow	MNC \uparrow	F1 (0.01) \uparrow	IoU \uparrow	IV \downarrow
Chairs	Vanilla PartSDF	3.567 ± 13.130	95.107 ± 4.402	96.790 ± 3.851	85.716 ± 10.951	$(1.788 \pm 5.729) \times 10^{-3}$
	S2MDF (QP) - PP	2.305 ± 12.704	94.791 ± 4.483	97.915 ± 3.278	89.186 ± 9.604	$(6.139 \pm 34.630) \times 10^{-9}$
	S2MDF (QP) - Train	2.700 ± 18.035	94.991 ± 4.085	98.089 ± 3.032	89.416 ± 9.361	$(8.117 \pm 40.900) \times 10^{-9}$
	S2MDF (Shift-All) - PP	2.206 ± 12.680	94.834 ± 4.472	98.003 ± 3.193	89.207 ± 9.606	$(6.663 \pm 30.730) \times 10^{-9}$
	S2MDF (Shift-All) - Train	2.173 ± 11.984	94.800 ± 4.437	98.063 ± 3.169	89.196 ± 9.407	$(7.320 \pm 26.150) \times 10^{-9}$
Mixers	Vanilla PartSDF	1.298 ± 6.284	88.102 ± 12.363	98.481 ± 7.898	76.667 ± 23.994	$(4.005 \pm 7.699) \times 10^{-5}$
	S2MDF (QP) - PP	1.300 ± 6.284	88.051 ± 12.447	98.480 ± 7.898	75.812 ± 24.337	$(1.333 \pm 4.423) \times 10^{-7}$
	S2MDF (QP) - Train	1.289 ± 6.767	88.032 ± 12.619	98.621 ± 7.950	76.419 ± 24.389	$(6.174 \pm 25.820) \times 10^{-9}$
	S2MDF (Shift-All) - PP	1.300 ± 6.284	88.051 ± 12.448	98.480 ± 7.898	75.812 ± 24.337	$(1.337 \pm 4.428) \times 10^{-7}$
	S2MDF (Shift-All) - Train	1.161 ± 5.533	88.137 ± 12.256	98.636 ± 7.216	76.435 ± 24.276	$(2.418 \pm 11.320) \times 10^{-8}$

Table 3: Shape reconstruction metrics for PartSDF on 100 chairs and mixers from the test set. Mean and standard deviations across shapes and parts.

one model on 100 chairs from PartNet [36], with 8 parts each, and a separate one on 100 mixers from [54], with 4 parts each. We then evaluate the models by freezing the weights and optimizing the latent codes on 100 chairs and 100 mixers from the test set, and we extract them with Marching Cubes at resolution 128. Notice that, while the mixers are made of watertight parts, the chairs are not, which serves as an interesting test for the robustness of our approaches to a scenario in which supervision is missing specifically at the intersection between parts. We report the results in Tab. 3 and Fig. 3, with additional results in the Appendix.

4.2 Experimental Protocol

In all three cases discussed above, we compare the original version of the method against four variant of our S2MDF layer: QP (PP) applies the QP-based layer only at meshing time, effectively as a post-processing step for the SDF values; QP (Train) appends the QP-based layer to the end of the network, affecting both training and inference; Shift-All (PP) and Shift-All (Train) apply the Shift-All approach in the same way, respectively as a post-processing step and during training.

4.3 Evaluation Metrics

To evaluate the results, we rely on metrics commonly used in 3D deep learning, along with one that computes intersection volume between objects and is key for assessing the validity of our method. When possible, we base them on point cloud to facet matches rather than point cloud to point cloud for increased accuracy, and thus we add a **Mesh** prefix to the metric.

Mesh Chamfer Distance. When measuring Chamfer Distance between two meshes M_1 and M_2 , point are uniformly sampled on the surface of the meshes: $P_1 \sim \mathcal{U}(M_1)$ and $P_2 \sim \mathcal{U}(M_2)$. However,

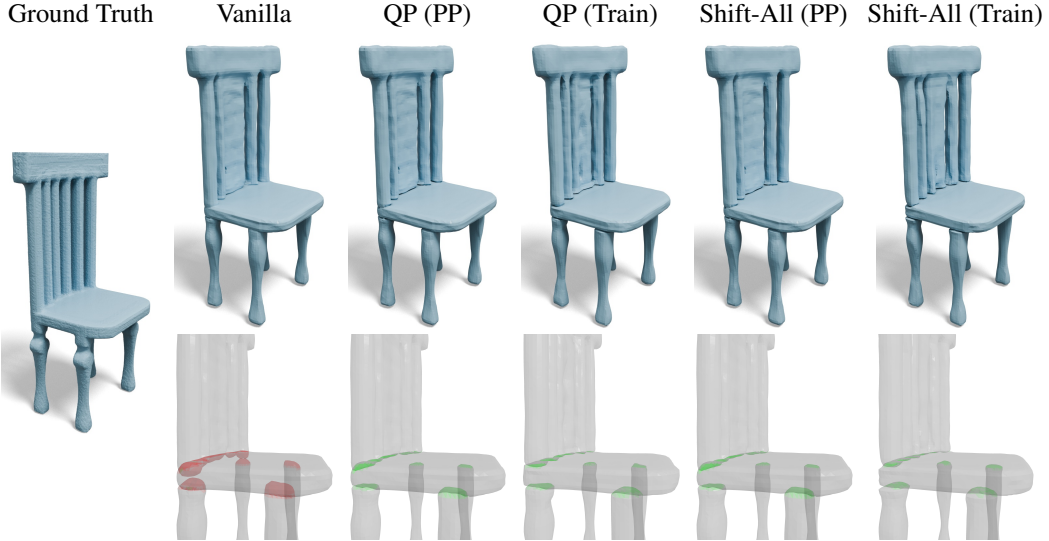


Figure 3: PartSDF [49] on PartNet [36] chairs: the top row shows ray-traced renderings, the bottom row visualizes intersections. Intersecting surfaces are in red, while touching surfaces are in green.

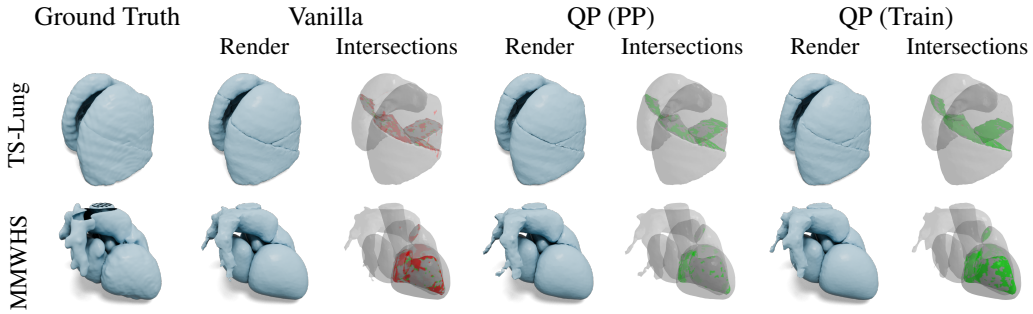


Figure 4: **Qualitative Comparisons.** We compare the outputs of the vanilla approach to our QP variants on MedTet. The vanilla variants have significant intersections (red), while the constrained ones have only contact regions (green).

this formulation is biased for a finite number of points (it is an overestimate), and inaccurate compared to finding the distance from a point to a mesh directly [46]. We therefore define Mesh Chamfer Distance using sampled point to mesh distances rather than point to point, as

$$d_{MCD}(M_1, M_2) = \frac{1}{|P_1|} \sum_{x \in P_1} \min_{y_m \in M_2} \|x - y_m\|_2^2 + \frac{1}{|P_2|} \sum_{y \in P_2} \min_{x_m \in M_1} \|x_m - y\|_2^2 \quad (7)$$

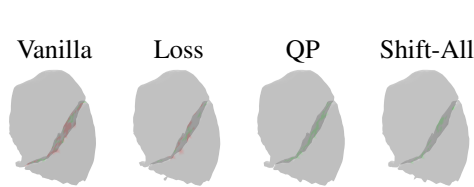


Figure 5: Qualitative visualization on left-lung layer during training for MedTet. The soft loss reconstructions. The loss term reduces the intersections compared to vanilla, but is far from completely satisfying non-intersection constraints.

Model	MCD ($\times 10^{-4}$) ↓	IV ↓
Vanilla	6.270 ± 0.201	$2.282 \pm 1.060 (\times 10^{-5})$
Loss	6.469 ± 0.372	$2.069 \pm 0.772 (\times 10^{-5})$
S2MDF (QP) - Train	6.096 ± 0.343	$1.352 \pm 0.544 (\times 10^{-9})$
S2MDF (Shift-All) - Train	6.469 ± 0.479	$7.412 \pm 10.603 (\times 10^{-12})$

Table 4: Metric comparison between the application of a soft intersection loss and our S2MDF layer during training for MedTet. The soft loss only marginally decreases the intersection volume, while our approach reduces it by several orders of magnitude.

Note that x_m and y_m can be anywhere on the mesh: a vertex, edge, or on the surface of any of its constituent triangles. This distance can be calculated efficiently.

Mesh Normal Consistency. Measures agreement between the normals of two point clouds with cosine similarity, using nearest neighbor matches as with the Chamfer Distance. As with the Mesh Chamfer Distance, we find the nearest points directly on the target mesh and use interpolated vertex normals rather than per-triangle flat normals.

F1 score (τ). As done in ObjectSDF++ [61], measures the ratio of points from M_1 at distance less than τ from M_2 . Precision is from predicted mesh to ground truth, recall is vice-versa, and F1 score is the harmonic mean of the two, being bidirectional. We once again measure distances with point-to-mesh approaches.

Mesh IOU. Measures the overall alignment between two meshes, as their volumetric intersection over union: $\frac{\text{vol}(M_1 \cap M_2)}{\text{vol}(M_1 \cup M_2)}$. We measure this approximately using a discrete voxel grid on the union bounding box of the two meshes.

Intersection Volume. The volume of the intersection between two meshes, M_1 and M_2 . This is calculated between predicted meshes for different parts of the same object or scene. It is always 0 in the ground truth.

4.4 Comparative Results

We execute experiments on single NVIDIA A100 or V100 GPUs, ensuring consistency when measuring times. We refer to the original papers for more details on the setup and the compute requirements. We report the results of our experiments in Tabs. 1 to 3 and Figs. 2 to 4 for MedTet, ObjectSDF++ and PartSDF respectively. Across all results, we observe that both QP and Shift-All reduce intersections by several orders of magnitude with respect to the original methods, including PartSDF and ObjectSDF++, which already include a loss term to mitigate them. The reduction in intersections is qualitatively visible in Figs. 2 to 4, where the red color indicates intersecting surfaces and the green color indicates touching surfaces. In terms of reconstruction quality, we observe that the metrics are quite noisy, but overall remain close to the original methods in mean and variance, with some exceptions. In particular, we notice that our S2MDF methods perform slightly better when used during training than only as a post-processing step, as the network can adapt to the constraint during training. We also notice that the Shift-All approach performs as well as the QP-based one during post-processing and slightly better during training, while being much faster. For few objects, like in the case of PartSDF mixers which only have 4 parts, QP does not add significant overhead when used as post-processing, however it increases the training time from 3h30m to 5h40m when used during training. For more complex objects, like the PartSDF chairs with 8 parts, the overhead of the QP-based approach is much more significant, increasing the training time from 4 to 9 hours for 2000 epochs, and the inference time from 20 to 60 seconds per object. On ObjectSDF++, where there are several dozens of objects per scene, the overhead of the QP-based approach makes it infeasible to use it during training. On the other hand, the Shift-All approach did not add any measurable overhead during training or post-processing in any of our tests, across all methods. As such, we recommend the use of S2MDF with the Shift-All approach.

Comparison against loss-based solutions To compare our method against loss-based intersection mitigations we run an experiment on TS-Lung for MedTet using the left lung only, where we apply an additional loss term to penalize intersections that does not exist in the base model: $\mathcal{L}_{inter} = \frac{1}{K-1} \sum_{k \neq min} \max(0, -(SDF_{min} + SDF_k))$. This equation penalizes overlapping geometry by enforcing that if a point is deeply inside one object ($SDF_{min} < 0$), it must be sufficiently outside all other objects ($SDF_k > 0$) so that their sum remains strictly positive. This loss is the same as the one applied in ObjectSDF++ and similar to the one in PartSDF and [27]. We show that the improvement offered by this loss in terms of intersection volume is marginal in Fig. 5 and Tab. 4, whereas our approach reduces it by several orders of magnitude. We did not remove this loss term from the other models tested in the paragraph above, since they explicitly include it in their formulation. This shows that our approach is compatible with it, as it can help regularizing the underlying field, but it still vastly improves the results.

Bringing intersections to zero To show that our approach is capable of fully eliminating intersections, we perform a small experiment comparing $\epsilon = 0$ and $\epsilon = 10^{-4}$ for the QP-based solution where we set $d_i + d_j \geq \epsilon$. We note that the first one evaluates to around 1.2×10^{-8} in terms of intersection volume, while the second one evaluates to exactly 0, showing that setting a small threshold effectively eliminates intersections, which can otherwise appear due to numerical errors.

Eikonal loss Regularization losses such as the eikonal loss are commonly used in SDF-based methods to encourage smoothness and regularity of the learned fields. We perform an ablation study on ObjectSDF++ to evaluate the effect of applying the Shift-All approach during training with and without a skip connection that allows the eikonal loss to be computed on the original network outputs. We observe that our layer performs overall similarly to the ground truth in both cases, but produces a noticeably lower MCD when the eikonal loss is applied to the original network output. We conjecture that regularization losses are better suited for the original field, as they help the network learn a naturally better field before applying the constraint layer. Thus, we suggest to apply regularization losses to the original field.

5 Conclusion

In this work, we have introduced a constrained SDF formulation to guarantee intersection-free multi-object implicit surface representations, and we have proposed S2MDF, a fast, plug-and-play module that can be applied to any object-compositional SDF-based representation to enforce the constraint, whose output remains compatible with linearly-interpolated meshing techniques. We have shown that our method eliminates them in theory and reduces them to numerical error in practice, without degrading the accuracy of the reconstructions and sometimes even improving it, which existing loss-based solutions cannot do. While we can address the numerical issue by adding a small margin to our constraint, an even more principled solution would be to design meshing algorithms that take into account multiple objects and can handle them correctly, which is a topic for future work.

References

- [1] P. Achlioptas, O. Diamanti, I. Mitliagkas, and L. Guibas. Learning Representations and Generative Models for 3D Point Clouds. pages 40–49, 2018.
- [2] Brandon Amos and J Zico Kolter. Optnet: Differentiable optimization as a layer in neural networks. In *International conference on machine learning*, pages 136–145. PMLR, 2017.
- [3] Antoine Bambade, Fabian Schramm, Adrien Taylor, and Justin Carpentier. Leveraging augmented-lagrangian techniques for differentiating over infeasible quadratic programs in machine learning. In *The Twelfth International Conference on Learning Representations*, 2024.
- [4] S. Boyd and L. Vandenberghe. *Convex Optimization*. Cambridge University Press, 2004.
- [5] S.L. Chan and E.O. Purisima. A new tetrahedral tessellation scheme for isosurface generation. *Computers & Graphics*, 22(1):83–90, 1998.
- [6] Rui Chen, Jianfeng Zhang, Yixun Liang, Guan Luo, Weiyu Li, Jiarui Liu, Xiu Li, Xiaoxiao Long, Jiashi Feng, and Ping Tan. Dora: Sampling and benchmarking for 3d shape variational auto-encoders. 2025.
- [7] Y. Chen, J. Yang, D. S. Mercadier, H. Le, and P. Fua. Medtet: An Online Motion Model for 4D Heart Reconstruction. 2024.
- [8] Z. Chen and H. Zhang. Learning Implicit Fields for Generative Shape Modeling. 2019.
- [9] J. Chibane, A. Mir, and G. Pons-Moll. Neural Unsigned Distance Fields for Implicit Function Learning. 2020.
- [10] C. Choy, D. Xu, J. Gwak, K. Chen, and S. Savarese. 3D-R2n2: A Unified Approach for Single and Multi-View 3D Object Reconstruction. pages 628–644, 2016.
- [11] A. Dai, C. Qi, and M. Nießner. Shape Completion Using 3D-Encoder-Predictor CNNs and Shape Synthesis. 2017.
- [12] B. Deng, S. Kulal, Z. Deng, C. Deng, Y. Tian, and J. Wu. Unsupervised Learning of Shape Programs with Repeatable Implicit Parts. 2022.
- [13] A. Doi and A. Koide. An Efficient Method of Triangulating Equivalued Surfaces by Using Tetrahedral Cells. *Transactopms on Information and Systems*, 74(1):214–224, 1991.
- [14] C. Dumery, A. Fan, R. Li, N. Talabot, and P. Fua. Enforcing View-Consistency in Class-Agnostic 3D Segmentation Fields. June 2025.
- [15] H. Fan, H. Su, and L. Guibas. A Point Set Generation Network for 3D Object Reconstruction from a Single Image. 2017.
- [16] Wenheng Ge, Tao Hu, Haoyu Zhao, Shu Liu, and Ying-Cong Chen. Ref-neus: Ambiguity-reduced neural implicit surface learning for multi-view reconstruction with reflection. 2023.
- [17] T. Groueix, M. Fisher, V. Kim, B. Russell, and M. Aubry. Atlasnet: A Papier-Mâché Approach to Learning 3D Surface Generation. 2018.
- [18] B. Guillard, E. Remelli, A. Lukoianov, S. Richter, T. Bagautdinov, P. Baque, and P. Fua. Deepmesh: Differentiable Iso-Surface Extraction. 46(11):7072–7087, 2024.
- [19] B. Guillard, F. Stella, and P. Fua. Meshudf: Fast and Differentiable Meshing of Unsigned Distance Field Networks. pages 576–592, 2022.
- [20] Z. Hao, H. Averbuch-Elor, N. Snavely, and S. Belongie. Dualsdf: Semantic Shape Manipulation Using a Two-Level Representation. pages 7631–7641, 2020.
- [21] Y. Jiang, D. Ji, Z. Han, and M. Zwicker. Sdfdiff: Differentiable Rendering of Signed Distance Fields for 3D Shape Optimization. 2020.
- [22] T. Ju, F. Losasso, S. Schaefer, and J. Warren. Dual Contouring of Hermite Data. 2002.

- [23] A. Kanazawa, S. Tulsiani, A. Efros, and J. Malik. Learning Category-Specific Mesh Reconstruction from Image Collections. 2018.
- [24] K. Karunratanakul, J. Yang, Y. Zhang, M. Black, K. Muandet, and S. Tang. Grasping Field: Learning Implicit Representations for Human Grasps. 2020.
- [25] Xin Kong, Shikun Liu, Marwan Taher, and Andrew J Davison. vmap: Vectorised object mapping for neural field slam. In *Proceedings of the IEEE/CVF Conference on Computer Vision and Pattern Recognition*, pages 952–961, 2023.
- [26] Zeqiang Lai, Yunfei Zhao, Haolin Liu, Zibo Zhao, Qingxiang Lin, Huiwen Shi, Xianghui Yang, Mingxin Yang, Shuhui Yang, Yifei Feng, et al. Hunyuan3d 2.5: Towards high-fidelity 3d assets generation with ultimate details. 2025.
- [27] H. Le, J. Xu, N. Talabot, J. Yang, and P. Fua. Pairwise-Constrained Implicit Functions for 3D Human Heart Modeling. 2025.
- [28] T. Lewiner, H. Lopes, A. W. Vieira, and G. Tavares. Efficient Implementation of Marching Cubes’ Cases with Topological Guarantees. In *Journal of Graphics Tools*, 2003.
- [29] Y.-T. Liu, L. Wang, J. Yang, W. Chen, X. Meng, B. Yang, and L. Gao. NeUDF: Learning Neural Unsigned Distance Fields with Volume Rendering. 2023.
- [30] Yuchun Liu, Benjamin Planche, Meng Zheng, Zhongpai Gao, Pierre Sibut-Bourde, Fan Yang, Terrence Chen, and Ziyang Wu. Implicit modeling of non-rigid objects with cross-category signals, 2023.
- [31] X. Long, C. Lin, L. Liu, Y. Liu, P. Wang, C. Theobalt, T. Komura, and W. Wang. Neuraludf: Learning Unsigned Distance Fields for Multi-View Reconstruction of Surfaces with Arbitrary Topologies. 2022.
- [32] W.E. Lorensen and H.E. Cline. Marching Cubes: A High Resolution 3D Surface Construction Algorithm. pages 163–169, 1987.
- [33] L. Mescheder, M. Oechsle, M. Niemeyer, S. Nowozin, and A. Geiger. Occupancy Networks: Learning 3D Reconstruction in Function Space. pages 4460–4470, 2019.
- [34] Ben Mildenhall, S. P. P., M. Tancik, J. T. Barron, R. Ramamoorthi, and R. Ng. NeRF: Representing Scenes as Neural Radiance Fields for View Synthesis. 2020.
- [35] P. Mittal, Y.-C. Cheng, M. Singh, and S. Tulsiani. AutoSDF: Shape Priors for 3D Completion, Reconstruction and Generation. 2022.
- [36] K. Mo, S. Zhu A. X., Chang, L. Yi, S. Tripathi, L. J. Guibas, and H. Su. PartNet: A Large-Scale Benchmark for Fine-Grained and Hierarchical Part-Level 3D Object Understanding. 2019.
- [37] M. Niemeyer and A. Geiger. GIRAFFE: Representing Scenes As Compositional Generative Neural Feature Fields. 2021.
- [38] J. Pan and K. Jia. Deep Mesh Reconstruction from Single RGB Images via Topology Modification Networks. 2019.
- [39] J. J. Park, P. Florence, J. Straub, R. A. Newcombe, and S. Lovegrove. DeepSDF: Learning Continuous Signed Distance Functions for Shape Representation. 2019.
- [40] S. Peng, C. Jiang, Y. Liao, M. Niemeyer, M. Pollefeys, and A. Geiger. Shape as Points: A Differentiable Poisson Solver. 2021.
- [41] D. Petrov, M. Gadelha, R. Měch, and E. Kalogerakis. ANISE: Assembly-Based Neural Implicit Surface Reconstruction. In *IEEE Transactions on Visualization and Computer Graphics*, 2023.
- [42] Tanweer Rashid, Sharmin Sultana, Mallar Chakravarty, and Michel Albert Audette. Atlas-based shared-boundary deformable multi-surface models through multi-material and two-manifold dual contouring. *Information*, 14(4), 2023.

- [43] E. Remelli, A. Lukoianov, S. Richter, B. Guillard, T. Bagautdinov, P. Baque, and P. Fua. Meshsdf: Differentiable Iso-Surface Extraction. 2020.
- [44] D. Ren, H. Shi, J. Zheng, and J. Cai. *Mcgrids: Monte Carlo-Driven Adaptive Grids For iso-Surface Extraction*, page 127144. Springer Nature Switzerland, September 2024.
- [45] T. Shen, J. Gao, K. Yin, M.-Y. Liu, and S. Fidler. Deep Marching Tetrahedra: A Hybrid Representation for High-Resolution 3D Shape Synthesis. 2021.
- [46] F. Stella, N. Talabot, H. Le, and P. Fua. High Resolution UDF Meshing via Iterative Networks. 2025.
- [47] Julian Straub, Thomas Whelan, Lingni Ma, Yufan Chen, Erik Wijmans, Simon Green, Jakob J. Engel, Raul Mur-Artal, Carl Ren, Shobhit Verma, Anton Clarkson, Mingfei Yan, Brian Budge, Yajie Yan, Xiaqing Pan, June Yon, Yuyang Zou, Kimberly Leon, Nigel Carter, Jesus Briales, Tyler Gillingham, Elias Mueggler, Luis Pesqueira, Manolis Savva, Dhruv Batra, Hauke M. Strasdat, Renzo De Nardi, Michael Goesele, Steven Lovegrove, and Richard Newcombe. The Replica dataset: A digital replica of indoor spaces. *arXiv preprint arXiv:1906.05797*, 2019.
- [48] T. Takikawa, J. Litalien, K. Yin, K. Kreis, C. Loop, D. Nowrouzezahrai, A. Jacobson, M. McGuire, and S. Fidler. Neural Geometric Level of Detail: Real-Time Rendering with Implicit 3D Shapes. 2021.
- [49] Nicolas Talabot, Olivier Clerc, Arda Cinar Demirtas, Alexis Goujon, Hieu Le, Doruk Oner, and Pascal Fua. PartSDF: Part-Based Implicit Neural Representation for Composite 3D Shape Parametrization and Optimization. October 2025.
- [50] M. Tancik, E. Weber, E. Ng, R. Li, B. Yi, J. Kerr, T. Wang, A. Kristoffersen, J. Austin, K. Salahi, A. Ahuja, D. McAllister, and A. Kanazawa. Nerfstudio: A Modular Framework for Neural Radiance Field Development. 2023.
- [51] K. Tertikas, D. Paschalidou, B. Pan J. J. and Park, M. A. Uy, I. Emiris, Y. Avrithis L., and Guibas. Generating Part-Aware Editable 3D Shapes Without 3D Supervision. 2023.
- [52] Graham M Treece, Richard W Prager, and Andrew H Gee. Regularised marching tetrahedra: improved iso-surface extraction. *Computers & Graphics*, 23(4):583–598, 1999.
- [53] Fuat Turk and Mahmut Kılıçaslan. Lung image segmentation with improved u-net, v-net and seg-net techniques. *PeerJ Computer Science*, 11:e2700, 2025.
- [54] S. Vasu, N. Talabot, A. Lukoianov, P. Baque, J. Donier, and P. Fua. Hybridsdf: Combining Free Form Shapes and Geometric Primitives for Effective Shape Manipulation. 2022.
- [55] B. Wang, C. Lu, and Y. Bo. DM-NeRF: 3D Scene Geometry Decomposition and Manipulation from 2D Images. 2023.
- [56] N. Wang, Y. Zhang, Z. Li, Y. Fu, W. Liu, and Y. Jiang. Pixel2mesh: Generating 3D Mesh Models from Single RGB Images. 2018.
- [57] P. Wang, L. Liu, Y. Liu, C. Theobalt, T. Komura, and W. Wang. Neus: Learning Neural Implicit Surfaces by Volume Rendering for Multi-View Reconstruction. 2021.
- [58] Jakob Wasserthal, Hanns-Christian Breit, Manfred T Meyer, Maurice Pradella, Daniel Hinck, Alexander W Sauter, Tobias Heye, Daniel T Boll, Joshy Cyriac, Shan Yang, et al. Totalsegmentator: Robust Segmentation of 104 Anatomic Structures in CT Images. *Radiology: Artificial Intelligence*, 2023.
- [59] J. Wu, C. Zhang, T. Xue, B. Freeman, and J. Tenenbaum. Learning a Probabilistic Latent Space of Object Shapes via 3D Generative-Adversarial Modeling. pages 82–90, 2016.
- [60] Qianyi Wu, Xian Liu, Yuedong Chen, Kejie Li, Chuanxia Zheng, Jianfei Cai, and Jianmin Zheng. Object-compositional neural implicit surfaces. In *European Conference on Computer Vision*, 2022.

- [61] Qianyi Wu, Kaisiyuan Wang, Kejie Li, Jianmin Zheng, and Jianfei Cai. Objectsdf++: Improved object-compositional neural implicit surfaces. In *Proceedings of the IEEE/CVF International Conference on Computer Vision*, pages 21764–21774, 2023.
- [62] R. Wu, Y. Zhuang, K. Xu, H. Zhang, and B. Chen. PQ-NET: A Generative Part Seq2seq Network for 3D Shapes. 2020.
- [63] Z. Wu, S. Song, A. Khosla, F. Yu, L. Zhang, X. Tang, and J. Xiao. 3D Shapenets: A Deep Representation for Volumetric Shapes. pages 1912–1920, 2015.
- [64] C. Xie, K. Park, R. Martin-Brualla, and M. Brown. FiG-NeRF: Figure-Ground Neural Radiance Fields for 3D Object Category Modelling, 2021.
- [65] Y. Yang, C. Feng, Y. Shen, and D. Tian. Foldingnet: Point Cloud Auto-Encoder via Deep Grid Deformation. June 2018.
- [66] Zehao Yu, Songyou Peng, Michael Niemeyer, Torsten Sattler, and Andreas Geiger. Monosdf: Exploring monocular geometric cues for neural implicit surface reconstruction. *Advances in Neural Information Processing Systems (NeurIPS)*, 2022.
- [67] X. Zeng, A. Vahdat, F. Williams, Z. Gojcic, O. Litany, S. Fidler, and K. Kreis. LION: Latent Point Diffusion Models for 3D Shape Generation. 2022.
- [68] B. Zhang, M. Nießner, and P. Wonka. 3DILG: Irregular Latent Grids for 3D Generative Modeling. 2022.
- [69] B. Zhang, J. Tang, M. Nießner, and P. Wonka. 3DShape2VecSet: A 3D Shape Representation for Neural Fields and Generative Diffusion Models. 2023.
- [70] C. Zhang, G. Lin, L. Yang, X. Li, T. Komura, S. Schaefer, J. Keyser, and W. Wang. Surface Extraction from Neural Unsigned Distance Fields. pages 0000–0000, October 2023.
- [71] Congyi Zhang, Mohamed Elgharib, Gereon Fox, Min Gu, Christian Theobalt, and Wenping Wang. An implicit parametric morphable dental model. *ACM Trans. Graph.*, 41(6), nov 2022.
- [72] Longwen Zhang, Ziyu Wang, Qixuan Zhang, Qiwei Qiu, Anqi Pang, Haoran Jiang, Wei Yang, Lan Xu, and Jingyi Yu. Clay: A controllable large-scale generative model for creating high-quality 3d assets. *ACM Transactions on Graphics*, 2024.
- [73] S. Zhi, T. Laidlow, S. Leutenegger, and A. Davison. In-Place Scene Labelling and Understanding with Implicit Scene Representation. 2021.
- [74] X. Zhuang. Multivariate Mixture Model for Myocardial Segmentation Combining Multi-Source Images. 41(12):2933–2946, 2018.

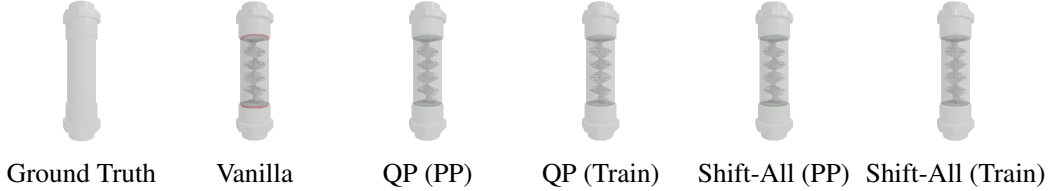


Figure A.1: PartSDF [49]: visualization of intersections. Intersecting surfaces are in red, while touching surfaces are in green.

A.1 Additional Results

We show here additional results and figures that were not included in the main text. In Fig. A.1, we show visualizations of the intersections for the PartSDF [49] experiment on the Mixers category. Similar conclusions as the main text apply.

A.1.1 Inference-time optimization on PartSDF

Contrary to the other methods we evaluate, PartSDF [49] is not limited to applying our S2MDF module either during training or as a post-processing step for the field at meshing time. Instead, it can also be applied during the inference-time optimization process that PartSDF performs to refine the geometry of each part, freezing the weights and optimizing the latent code. In Tabs. A.1 and A.2, we present quantitative results for the same PartSDF [49] experiment as in Tab. 3, additionally comparing the application of S2MDF during the inference-time optimization ("Optim"). We observe that, while not disrupting the optimization process, applying S2MDF during the optimization does not provide advantages over applying it during training or as a simple post-processing step, and it is outperformed by both. This is reasonable, as the network weights have been trained without such layer, and the resulting latent space may not be optimal to allow for a good optimization with the S2MDF module.

	MCD ($\times 10^{-4}$) ↓	NC ↑	F1 (0.001) ↑	IoU ↑	IV ↓
Vanilla PartSDF	3.567 ± 13.130	95.107 ± 4.402	96.790 ± 3.851	85.716 ± 10.951	(1.788 ± 5.729) $\times 10^{-3}$
S2MDF (Shift-All) - PP	2.206 ± 12.680	94.834 ± 4.472	98.003 ± 3.193	89.207 ± 9.606	(6.663 ± 30.730) $\times 10^{-9}$
S2MDF (QP) - PP	2.305 ± 12.704	94.791 ± 4.483	97.915 ± 3.278	89.186 ± 9.604	(6.139 ± 34.630) $\times 10^{-9}$
S2MDF (Shift-All) - Optim	2.838 ± 21.485	94.898 ± 4.474	98.110 ± 3.338	89.686 ± 9.737	(3.550 ± 32.310) $\times 10^{-9}$
S2MDF (QP) - Optim	2.801 ± 20.365	94.871 ± 4.388	98.081 ± 3.254	89.628 ± 9.801	(4.145 ± 27.200) $\times 10^{-9}$
S2MDF (Shift-All) - Train	2.173 ± 11.984	94.800 ± 4.437	98.063 ± 3.169	89.196 ± 9.407	(7.320 ± 26.150) $\times 10^{-9}$
S2MDF (QP) - Train	2.700 ± 18.035	94.991 ± 4.085	98.089 ± 3.032	89.416 ± 9.361	(8.117 ± 40.900) $\times 10^{-9}$

Table A.1: Shape reconstruction metrics for PartSDF on 100 chairs from the test set. Mean and standard deviations across shapes and parts.

	MCD ($\times 10^{-4}$) ↓	NC ↑	F1 (0.001) ↑	IoU ↑	IV ↓
Vanilla PartSDF	1.298 ± 6.284	88.102 ± 12.363	98.481 ± 7.898	76.667 ± 23.994	(4.005 ± 7.699) $\times 10^{-5}$
S2MDF (Shift-All) - PP	1.300 ± 6.284	88.051 ± 12.448	98.480 ± 7.898	75.812 ± 24.337	(1.337 ± 4.428) $\times 10^{-7}$
S2MDF (QP) - PP	1.300 ± 6.284	88.051 ± 12.447	98.480 ± 7.898	75.812 ± 24.337	(1.333 ± 4.423) $\times 10^{-7}$
S2MDF (Shift-All) - Optim	1.296 ± 6.208	88.137 ± 12.392	98.481 ± 7.868	76.483 ± 24.039	(3.974 ± 28.770) $\times 10^{-9}$
S2MDF (QP) - Optim	1.303 ± 6.240	88.129 ± 12.405	98.476 ± 7.890	76.482 ± 24.037	(4.101 ± 28.890) $\times 10^{-9}$
S2MDF (Shift-All) - Train	1.161 ± 5.533	88.137 ± 12.256	98.636 ± 7.216	76.435 ± 24.276	(2.418 ± 11.320) $\times 10^{-8}$
S2MDF (QP) - Train	1.289 ± 6.767	88.032 ± 12.619	98.621 ± 7.950	76.419 ± 24.389	(6.174 ± 25.820) $\times 10^{-9}$

Table A.2: Shape reconstruction metrics for PartSDF on 100 mixers from the test set. Mean and standard deviations across shapes and parts.

A.2 Proofs

A.2.1 Theorem 1 (Constraint Equivalence for SDFs)

A vector-valued $SDF = [SDF_1, \dots, SDF_K] : \mathbb{R}^3 \rightarrow \mathbb{R}^K$ satisfies constraint $\min^{(2)}(\mathbf{u}) \geq 0$ at every point $\mathbf{p} \in \mathbb{R}^3$, with $\mathbf{u} = SDF(\mathbf{p})$, if and only if it satisfies $\min^{(1)}(\mathbf{u}) + \min^{(2)}(\mathbf{u}) \geq 0$ at every point $\mathbf{p} \in \mathbb{R}^3$.

Proof. Through the second constraint and the definition of $\min^{(n)}$, we have both $\min^{(2)}(\mathbf{u}) \geq -\min^{(1)}(\mathbf{u})$ and $\min^{(2)}(\mathbf{u}) \geq \min^{(1)}(\mathbf{u})$ and, therefore, $\min^{(2)}(\mathbf{u}) \geq 0$ at every point $\mathbf{p} \in \mathbb{R}^3$.

For the inverse implication, we consider an arbitrary point $\mathbf{p} \in \mathbb{R}^3$. If \mathbf{p} lies outside all objects, the second condition is trivially satisfied as all SDFs are positive. If it is inside an object, we can use the Lipschitz continuity of SDFs to show that the second constraint must also be satisfied.

For this, we first define some notation for point \mathbf{p} with SDF vector \mathbf{u} . Let:

- a and b be the indices of the objects with the smallest and second smallest SDF, respectively.
- \mathbf{y}_a and \mathbf{y}_b be points on the surfaces of these objects that are closest to \mathbf{p} .
- $s_a : \mathbb{R}^3 \rightarrow \mathbb{R}$ and $s_b : \mathbb{R}^3 \rightarrow \mathbb{R}$ be the signed distance functions of these objects.

Based on the definition of SDFs of Equation (1) and using the first constraint, we can write

$$\begin{aligned} \min^{(1)}(\mathbf{u}) &= s_a(\mathbf{p}) = -\|\mathbf{p} - \mathbf{y}_a\| \text{ and} \\ \min^{(2)}(\mathbf{u}) &= s_b(\mathbf{p}) = \|\mathbf{p} - \mathbf{y}_b\|. \end{aligned}$$

Using that SDFs are 1-Lipschitz continuous, we have

$$\begin{aligned} s_a(\mathbf{y}_b) - s_a(\mathbf{p}) &\leq |s_a(\mathbf{y}_b) - s_a(\mathbf{p})| \leq \|\mathbf{y}_b - \mathbf{p}\| \\ \Leftrightarrow s_a(\mathbf{y}_b) &\leq s_a(\mathbf{p}) + \|\mathbf{y}_b - \mathbf{p}\| \\ &= s_a(\mathbf{p}) + s_b(\mathbf{p}) \\ &= \min^{(1)}(\mathbf{u}) + \min^{(2)}(\mathbf{u}) \end{aligned}$$

Suppose now that the second constraint is not satisfied at \mathbf{p} . Then

$$s_a(\mathbf{y}_b) \leq \min^{(1)}(\mathbf{u}) + \min^{(2)}(\mathbf{u}) < 0,$$

which means that \mathbf{y}_b , a point on the surface of object b , is strictly inside a . Thus, in its vicinity, there must be a point that is both within object a and b , which is impossible as it violates the first constraint. Therefore, there cannot be any point \mathbf{p} such that the second constraint is not satisfied. \square

A.2.2 Sum of two mins is equivalent to pairwise sums

Consider an arbitrary vector $\mathbf{d} \in \mathbb{R}^K$ and its elements d_i , $1 \leq i \leq K$. We claim that $\min^{(2)}(\mathbf{d}) + \min^{(1)}(\mathbf{d}) \geq 0$ if and only if $d_i + d_j \geq 0$, $1 \leq i < j \leq K$.

Proof. Because the $\min^{(2)}$, $\min^{(1)}$ and the set of all pairwise sums are invariant under permutation of elements, we can assume without loss of generality that the elements of \mathbf{d} are sorted in ascending order $\mathbf{d} = (d_1, d_2, \dots, d_K)$, $d_1 \leq d_2 \leq \dots \leq d_K$.

Forward Proof. We are given that $\min^{(1)}(\mathbf{d}) + \min^{(2)}(\mathbf{d}) \geq 0$, i.e. $d_1 + d_2 \geq 0$.

- Given $i \geq 1$, it follows that $d_i \geq d_1$.

- As $j > i \geq 1, j \geq 2$. It follows that $d_j \geq d_2$.

We can combine the two inequalities to get $d_i + d_j \geq d_1 + d_2$. This completes the forward proof.

Backward Proof. We are given that $d_i + d_j \geq 0, 1 \leq i < j \leq K$. We can set $i = 1$ and $j = 2$, meaning $d_1 + d_2 \geq 0$. Because $\min^{(1)}(\mathbf{d}) = d_1$ and $\min^{(2)}(\mathbf{d}) = d_2$, it follows that $\min^{(2)}(\mathbf{d}) + \min^{(1)}(\mathbf{d}) \geq 0$. This completes the backward proof. \square

A.2.3 Theorem 2

Given the vector-valued SDFs $\mathbf{d}_1 \in \mathbb{R}^K$ and $\mathbf{d}_2 \in \mathbb{R}^K$, if they both satisfy the MDF constraint (Eq. Eq. (3)), i.e. $\min^{(1)}(\mathbf{d}) + \min^{(2)}(\mathbf{d}) \geq 0$, we claim any linearly interpolated point between them $\mathbf{d}_\alpha = \alpha\mathbf{d}_1 + (1 - \alpha)\mathbf{d}_2$ for $\alpha \in [0, 1]$ also satisfies this constraint.

Proof. For notational convenience, let $S_2(\mathbf{d}) = \min^{(1)}(\mathbf{d}) + \min^{(2)}(\mathbf{d})$, allowing us to state the constraint as $S_2(\mathbf{d}) \geq 0$. Example 3.6, p. 80 in [4] proves that the function $f_r(\mathbf{d})$, representing the sum of the r largest components of a vector, is convex. The sum of the r smallest components can be expressed as $S_r(\mathbf{d}) = -f_r(-\mathbf{d})$. Since f_r is convex, $f_r(-\mathbf{d})$ is convex, and its negation $-f_r(-\mathbf{d})$ is concave. Because S_2 is a special case of S_r , it is also concave. Using the definition of concavity for $\alpha \in [0, 1]$:

$$S_2(\mathbf{d}_\alpha) = S_2(\alpha\mathbf{d}_1 + (1 - \alpha)\mathbf{d}_2) \geq \alpha S_2(\mathbf{d}_1) + (1 - \alpha)S_2(\mathbf{d}_2) \quad (8)$$

Since $S_2(\mathbf{d}_1) \geq 0$ and $S_2(\mathbf{d}_2) \geq 0$, and both α and $(1 - \alpha)$ are non-negative, it follows that $\alpha S_2(\mathbf{d}_1) + (1 - \alpha)S_2(\mathbf{d}_2) \geq 0$. Thus, $S_2(\mathbf{d}_\alpha) \geq 0$, guaranteeing that \mathbf{d}_α always satisfies the MDF constraint Eq. (3). The same cannot be said for the constraint $\min^{(2)}(\mathbf{d}) \geq 0$, as $\min^{(2)}$ is not concave, meaning $\min^{(2)}(\alpha\mathbf{d}_1 + (1 - \alpha)\mathbf{d}_2) \not\geq \alpha \min^{(2)}(\mathbf{d}_1) + (1 - \alpha) \min^{(2)}(\mathbf{d}_2)$. Thus, a linearly interpolated point could break the constraint. \square

A.2.4 Line Crossing

Given the vector-valued SDFs $\mathbf{d}_1 \in \mathbb{R}^K$ and $\mathbf{d}_2 \in \mathbb{R}^K$ at points, if they both satisfy the MDF constraint (Eq. Eq. (3)), i.e. $\min^{(1)}(\mathbf{d}) + \min^{(2)}(\mathbf{d}) \geq 0$, and an edge between them is linearly interpolated by a meshing algorithm for surface reconstruction, we claim that there are at most two object surfaces between these points and that these surfaces do not cross.

Proof. We already know from Theorem Theorem 1 that $\min^{(1)}(\mathbf{d}) + \min^{(2)}(\mathbf{d}) \geq 0$ implies $\min^{(2)}(\mathbf{d}) \geq 0$, which implies a vector \mathbf{d} satisfying this constraint can have at most one negative one value.

Let us assume for now that neither of the two vectors contain zero values. Let us perform a case analysis on the possibilities of the signs of the values of the two vectors:

- Neither \mathbf{d}_1 nor \mathbf{d}_2 contain negative values. In this case, there are no object surfaces between them.
- One of them has a negative value. In this case, there is only one object surface, and we are outside every other object.
- Both of them have a negative value, and these negative values are in the same index i . In this case, both points are inside the same object and there will be no surface between them.
- Both of them have a negative value, and these are in different indices, i and j . Then, there will be two zero-crossings and two object surfaces.

The first three cases have no risk of having two surfaces intersect, so our interest is in the final case. Let $\mathbf{d}_1 = \mathbf{p}$ and $\mathbf{d}_2 = \mathbf{q}$ for notational convenience, and i, j be the minimum indices in \mathbf{p} and \mathbf{q} , respectively. Then, $p_i < 0$ and $q_j < 0$. We know from Appendix A.2.2 that satisfaction of the MDF constraint implies all pairwise sums in a vector are positive. Thus, we have that:

$$p_i < 0, p_i + p_j \geq 0 \implies p_j > 0 \quad (9)$$

$$q_j < 0, q_i + q_j \geq 0 \implies q_i > 0 \quad (10)$$

Surfaces along the line segment will appear at zero-crossings. If we parameterize points along this segment with $\alpha \in [0, 1]$, assuming $\alpha = 0$ at the point where \mathbf{p} is evaluated, and $\alpha = 1$ for \mathbf{q} , we can find the zero-crossing for both object i and j :

$$\alpha_i = \frac{-p_i}{q_i - p_i} \quad (11)$$

$$\alpha_j = \frac{-p_j}{q_j - p_j} \quad (12)$$

We will now derive the relationship between α_i and α_j based on Eqs. Eq. (9) and Eq. (10). Given $p_j > 0$, we divide $p_i + p_j \geq 0$ to obtain $\frac{p_i}{p_j} + 1 \geq 0$. Rearranging this, and with the knowledge that $p_i < 0$, we obtain the bounds:

$$1 \geq -\frac{p_i}{p_j} > 0 \quad (13)$$

With a similar approach, dividing by $q_i + q_j \geq 0$ by $q_i > 0$, we can also obtain:

$$1 \geq -\frac{q_j}{q_i} > 0 \quad (14)$$

Multiplying both inequalities:

$$1 \geq \frac{p_i q_j}{p_j q_i} > 0 \quad (15)$$

Since $p_j > 0$ and $q_i > 0$, $p_j q_i > 0$ and we can multiply both sides with it, dropping the lower bound:

$$p_j q_i \geq p_i q_j \quad (16)$$

Now, subtract $p_i p_j$ from both sides and factor:

$$p_j(q_i - p_i) \geq p_i(q_j - p_j) \quad (17)$$

We know $p_i < 0$ and $q_i > 0$, so $q_i - p_i > 0$, we divide both sides:

$$p_j \geq (q_j - p_j) \frac{p_i}{q_i - p_i} \quad (18)$$

Similarly, $p_j > 0$ and $q_j < 0$, so $q_j - p_j < 0$, divide both sides and flip the inequality:

$$\frac{p_j}{q_j - p_j} \leq \frac{p_i}{q_i - p_i} \quad (19)$$

Multiply both sides by -1:

$$-\frac{p_j}{q_j - p_j} \geq -\frac{p_i}{q_i - p_i} \quad (20)$$

And we finally obtain α_i and α_j :

$$\alpha_j \geq \alpha_i \implies \alpha_i \leq \alpha_j \quad (21)$$

This proves that the surface of the object j will always be closer to the point where \mathbf{q} is evaluated than object i . The surfaces can at most touch each other, or will be disjoint. This completes our proof in the case where neither of the vectors contain zero values. If they do contain zero values, the following cases can happen:

- One of the vectors $\mathbf{d}_1, \mathbf{d}_2$ has one or more zero values, let us assume \mathbf{d}_1 , and the other vector does not. A surface point will be placed exactly at the point where \mathbf{d}_1 is evaluated. Due to Eq. (3), the zero value in \mathbf{d}_1 implies the absence of negative values in \mathbf{d}_1 , which in turn implies that its point is on the surface of one or more objects but outside every other object.

- Both vectors have one or more zero values in the same indices. This implies that one or more surfaces lie exactly on the line segment, which does not cause a crossing.
- Both vectors have one or more zero values, and these zero values are potentially in different indices. This implies the presence of multiple surface points at the points where the vectors are evaluated, however neither of the vectors can have negative values, due to Eq. (3), which implies that both points are on the surface of one or more objects but outside every other object.

□

A.2.5 QP analytical solution for the two-object case

Given the optimization problem:

$$\text{minimize } \|\mathbf{d} - \mathbf{u}\|^2 \quad \text{subject to } \min^{(1)}(\mathbf{d}) + \min^{(2)}(\mathbf{d}) \geq 0. \quad (22)$$

in two dimensions, i.e. $\mathbf{d} \in \mathbb{R}^2$, its optimal solution is equivalent to Shift-All, i.e. not changing \mathbf{u} in the satisfied case, and shifting both variables by $-(\min^{(1)}(\mathbf{u}) + \min^{(2)}(\mathbf{u}))/2$ in the unsatisfied case.

Proof. Let us state the common way to formulate an optimization problem with inequality constraints:

$$\text{minimize } f(\mathbf{d}) \quad \text{subject to } g(\mathbf{d}) \leq 0. \quad (23)$$

Let $\mathbf{u} = (u_1, u_2)$ and $\mathbf{d} = (d_1, d_2)$. As there are only two elements, $\min^{(1)}(\mathbf{d}) + \min^{(2)}(\mathbf{d}) = d_1 + d_2 \geq 0 \implies -d_1 - d_2 \leq 0$.

Then, for our case, $f(\mathbf{d}) = \|\mathbf{d} - \mathbf{u}\|^2 = (d_1 - u_1)^2 + (d_2 - u_2)^2$ and $g(\mathbf{d}) = -d_1 - d_2$. Let's define the Lagrangian function:

$$\mathcal{L}(\mathbf{d}, \lambda) = f(\mathbf{d}) + \lambda g(\mathbf{d}) = (d_1 - u_1)^2 + (d_2 - u_2)^2 - \lambda(d_1 + d_2) \quad (24)$$

We now write down the KKT conditions:

1. **Stationarity:** $\nabla f(\mathbf{d}^*) + \lambda \nabla g(\mathbf{d}^*) = 0$.
2. **Primal feasibility:** $g(\mathbf{d}^*) \leq 0$.
3. **Dual feasibility:** $\lambda \geq 0$.
4. **Complementary slackness:** $\lambda g(\mathbf{d}^*) = 0$.

Before continuing our solution, we derive the gradients:

$$\nabla f(\mathbf{d}) = 2 \begin{bmatrix} d_1 - u_1 \\ d_2 - u_2 \end{bmatrix}, \quad \nabla g(\mathbf{d}) = \begin{bmatrix} -1 \\ -1 \end{bmatrix} \quad (25)$$

Inactive case. Assume $g(\mathbf{d}^*) < 0$, meaning the constraint is already satisfied. Then, by stationarity, $\nabla f(\mathbf{d}^*) = 0$:

$$\nabla f(\mathbf{d}^*) = 2 \begin{bmatrix} d_1^* - u_1 \\ d_2^* - u_2 \end{bmatrix} = \begin{bmatrix} 0 \\ 0 \end{bmatrix} \implies d_1^* = u_1, d_2^* = u_2, \mathbf{d}^* = \mathbf{u} \quad (26)$$

By complementary slackness, $\lambda = 0$. Let us check the feasibility:

- **Primal:** $g(\mathbf{d}^*) = g(\mathbf{u}) = -u_1 - u_2 < 0 \implies u_1 + u_2 > 0$.
- **Dual:** $\lambda = 0 \geq 0$, satisfied.

Feasibilities are satisfied and the inactive solution is valid when $u_1 + u_2 > 0$. The solution intuitively makes sense, as our projection does not need to modify the initial value \mathbf{u} in case the constraint is already satisfied.

Active case. Assume $g(\mathbf{d}^*) = 0$, meaning the the solution is at the constraint boundary. By complementary slackness:

$$\lambda g(\mathbf{d}^*) = -\lambda(d_1^* + d_2^*) = 0 \implies d_2^* = -d_1^* \quad (27)$$

By stationarity, $\nabla f(\mathbf{d}^*) + \lambda \nabla g(\mathbf{d}^*) = 0$, and substituting the above $d_2^* = -d_1^*$:

$$2 \begin{bmatrix} d_1^* - u_1 \\ -d_1^* - u_2 \end{bmatrix} - \lambda \begin{bmatrix} 1 \\ 1 \end{bmatrix} = \begin{bmatrix} 0 \\ 0 \end{bmatrix} \implies \begin{aligned} d_1^* - u_1 &= \lambda/2 \\ -d_1^* - u_2 &= \lambda/2 \end{aligned} \quad (28)$$

Summing the two equations, we get $\lambda = -(u_1 + u_2)$. We can plug this result back into the equations to derive \mathbf{d}^* :

$$d_1^* = u_1 + \frac{\lambda}{2} = u_1 - \frac{u_1 + u_2}{2} \quad (29)$$

$$d_2^* = u_2 + \frac{\lambda}{2} = u_2 - \frac{u_1 + u_2}{2} \quad (30)$$

Let's consider the feasibilities:

- **Primal:** $g(\mathbf{d}^*) = -d_1^* - d_2^* = -u_1 + \frac{u_1+u_2}{2} - u_2 + \frac{u_1+u_2}{2} = 0 \leq 0$, satisfied.
- **Dual:** $\lambda = -u_1 - u_2 \geq 0 \implies u_1 + u_2 \leq 0$.

Feasibilities are satisfied and the inactive solution is valid when $u_1 + u_2 \leq 0$, meaning both values need to be shifted by $-\frac{u_1 + u_2}{2}$ when the constraint is not satisfied on \mathbf{u} .

Because our objective function $f(\mathbf{d}) = \|\mathbf{d} - \mathbf{u}\|^2$ is strictly convex and the inequality constraint $g(\mathbf{d}) = -d_1 - d_2 \leq 0$ is affine, the optimization problem is strictly convex. Under these conditions, the KKT conditions are both necessary and sufficient for the \mathbf{d}^* we derived to be the **global optimum** [4, Section 5.5.3, p. 244].

This analytical solution leads to the exact same formulations as our Shift-All. □

A.2.6 Solution to the modified QP problem

Let $\mathbf{u} \in \mathbb{R}^K$ be the K -dimensional SDF vector at a point in space, the following optimization problem: given the optimization problem:

$$\begin{aligned} &\text{minimize} && \|\mathbf{d} - \mathbf{u}\|^2 && (31a) \\ &\mathbf{d} \in \mathbb{R}^K \end{aligned}$$

$$\text{subject to} \quad \min^{(1)}(\mathbf{d}) + \min^{(2)}(\mathbf{d}) > 0, \quad (31b)$$

$$\mathbf{d}_i - \mathbf{d}_j = \mathbf{u}_i - \mathbf{u}_j, \forall i, j \in [K], i < j \quad (31c)$$

has Shift-All as its optimal solution, i.e. not changing \mathbf{u} in the satisfied case, and shifting all variables by $-(\min^{(1)}(\mathbf{u}) + \min^{(2)}(\mathbf{u}))/2$ in the unsatisfied case.

Proof. The unconstrained minimizer of the objective function is $\mathbf{d} = \mathbf{u}$. If \mathbf{u} satisfies the MDF constraint, then $\mathbf{d} = \mathbf{u}$ is also the optimal solution to the constrained problem.

If \mathbf{u} does not satisfy the MDF constraint, we notice that the second constraint forces solutions to be of the form $\mathbf{d} = \mathbf{u} + c\mathbf{1}$, where $\mathbf{1}$ is the vector of all ones. For simplicity, we define $\mathbf{d}_m = \min^{(1)}(\mathbf{d})$ and $\mathbf{d}_n = \min^{(2)}(\mathbf{d})$. Then, we have that:

$$\mathbf{d}_m = \mathbf{u}_m + c \quad (32)$$

$$\mathbf{d}_n = \mathbf{u}_n + c \quad (33)$$

From the first constraint of the optimization problem, it follows that:

$$\mathbf{d}_m + \mathbf{d}_n = \mathbf{u}_m + \mathbf{u}_n + 2c \geq 0 \implies c \geq -\frac{\mathbf{u}_m + \mathbf{u}_n}{2} \quad (34)$$

The objective function is convex so, if its global minimum is not feasible, the optimal solution \mathbf{d}^* will be at the boundary of the feasible region. In fact, if it wasn't at the boundary, then it would be in the interior of the feasible region. In such case, $\nabla \|\mathbf{d} - \mathbf{u}\|^2 = 2(\mathbf{d} - \mathbf{u}) = 0$ at \mathbf{d}^* , otherwise it would not be optimal, but this implies that $\mathbf{d}^* = \mathbf{u}$, which is not feasible. Therefore, \mathbf{d}^* must be at the boundary, meaning $c = -\frac{\mathbf{u}_m + \mathbf{u}_n}{2}$.

In short, if \mathbf{u} satisfies the MDF constraint, then $\mathbf{d}^* = \mathbf{u}$ is the optimal solution. If \mathbf{u} does not satisfy the MDF constraint, then $\mathbf{d}^* = \mathbf{u} - \frac{\min^{(1)}(\mathbf{u}) + \min^{(2)}(\mathbf{u})}{2} \mathbf{1}$ is the optimal solution. This is exactly the Shift-All solution as defined in the main text.

□